entropy

MDPI

Article

Optimization of Two-Phase Ejector Mixing Chamber Length under Varied Liquid Volume Fraction

Jia Yan [1], Yuetong Shu [1], Jing Jiang [2,*] and Huaqin Wen [1]

1 School of Civil Engineering and Architecture, Southwest University of Science and Technology, Mianyang 621010, China
2 School of Artificial Intelligence, Yantai Institute of Technology, Yantai 264003, China
* Correspondence: jackjiangyt@163.com

Abstract: The ejector performance varies with the mixing chamber length which is largely dependent on the fluid liquid volume fraction at the inlet. In this study, numerical simulations are conducted to optimize two mixing chamber lengths of a two-phase ejector under varied liquid volume fractions of 0–0.1 in two inlet fluids. The main findings are as follows: (1) The two optimal lengths of constant-pressure and constant-area mixing chambers are identified within 23–44 mm and 15–18 mm, respectively, when the primary inlet fluid is in two-phase; (2) the two optimal lengths are 2–5 mm and 9–15 mm, respectively, when the secondary inlet fluid is in two-phase; (3) when both inlets are in two-phase, the two optimal lengths are ranged in 5–23 mm and 6–18 mm; (4) little liquid within inlet fluid has a significant influence on ejector performances; and (5) optimal constant-pressure mixing chamber length and the sum of the two optimal lengths increase with the primary flow inlet liquid volume fraction but decrease with that of the secondary flow inlet.

Keywords: ejector; entrainment ratio; liquid volume fraction; numerical simulation; mixing chamber length

Citation: Yan, J.; Shu, Y.; Jiang, J.; Wen, H. Optimization of Two-Phase Ejector Mixing Chamber Length under Varied Liquid Volume Fraction. *Entropy* **2023**, *25*, 7. https://doi.org/10.3390/e25010007

Academic Editor: Jean-Noël Jaubert

Received: 20 November 2022
Revised: 12 December 2022
Accepted: 16 December 2022
Published: 21 December 2022

1. Introduction

With the rapid development of technology, energy consumption has restricted economic and social development. Therefore, it is quite urgent to improve energy efficiency in air-conditioning and refrigeration devices [1,2]. Various studies have been conducted to improve the performance of refrigeration systems and thus solve environmental issues [3–5]. Moreover, the performance of refrigeration systems has been enhanced by adopting advanced technologies [6–9]. For the refrigeration needed in refrigerated trucks that always need air-conditioning services and refrigerating or freezing purposes for food storage, a pressure regulating valve (PRV) is equipped between two evaporators to keep the required pressure difference [10,11], which causes many irreversible throttling losses. Therefore, an ejector is used to replace the PRV and partially recover the throttling losses [12–14]. The schematic of a typical simplified EMERS with two temperature levels is shown in Figure 1 [15]. An EMERS has some advantages such as low operating costs [16,17].

When the EMERS is used in refrigerated trucks, the essential device of the system is the ejector [18,19]. The two flows of the refrigerant flows mix in the ejector and enter the compressor with a pressure lift [20]. By optimizing the area ratio (AR) and the nozzle exit position (NXP) and so on, ejector performance can be improved [21,22].

High entrainment performance of the ejector can be achieved if the two flows are mixed well [23]. Nakagawa et al. [24] studied the effect of mixing the length of a transcritical CO_2 two-phase ejector with a rectangular cross-section, and they claimed that the 15 mm of mixing length can produce good ejector performance. Sarkar et al. [25] showed that the constant-area mixing chamber cross-section area affects ejector performance mainly depending on the ejector inlet conditions. Banasiak et al. [26] also proved that the ejector performance largely depends on the mixing chamber length in a small ejector-based

R744 transcritical heat pump system. Jeon et al. [27] studied an ejector mixing length and improved system performance. Fu et al. [28] optimized the mixing chamber throat diameter to improve the steam ejector performance. By using three-dimensional numerical simulations, Dong et al. [29] studied the effects of the mixing chamber length, and the best ejector performance was obtained within a certain range of the mixing chamber length.

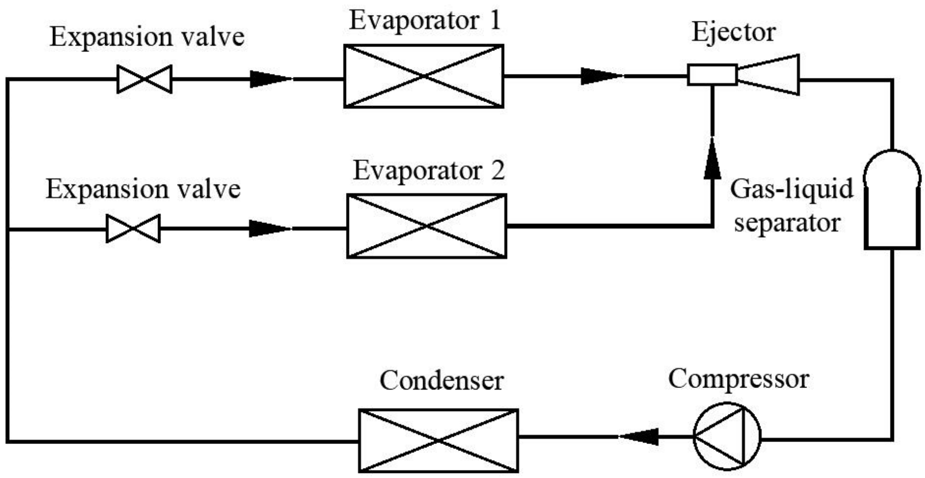

Figure 1. Schematic of a two-temperature evaporator-based EMERS.

In many cases, the ejector operates with a gas-liquid mixture of primary flow or gas-liquid mixture of secondary flow. Hemidi et al. [30] conducted the study when the water droplets were ejected into primary air flow, which improved off-design performance. Yuan et al. [31] investigated a two-phase ejector experimentally and numerically. Similarly, according to the study of Yuan et al. [31], Chen et al. [32] also studied the two-phase secondary flow ejector performance. They claimed that ER and PRR would decrease when the induced flow is accompanied by water. Aliabadi et al. [33] investigated the effects of primary nozzle inlet wetness in the range of 0–1%. Their results indicate that the water droplets make an ER improvement.

To the best of the authors' knowledge, there is no study on the effects of mixing chamber length under different liquid volume fractions (LVF) which means the liquid volume percentage in the two-phase flow on ejector performance used refrigerant of $C_2H_2F_4$ as displayed in Figure 1. With our former study [15], it was known that when the LVF of the two inlet flows varies, it may have an undesirable effect on ejector performance, and thus, the ejector with original geometries may be in malfunction.

Thus, this study aims to optimize the constant-pressure mixing section length (L_{pm}) and constant-area mixing section length (L_{am}) of a two-phase ejector under different primary and secondary flow liquid volume fractions. The details of the work in this paper are:

- to identify optimal L_{pm} under varied secondary flow liquid volume fraction;
- to find the optimal L_{pm} under varied primary flow liquid volume fraction;
- with optimal L_{pm}, to search for the optimal L_{am} under varied secondary flow liquid volume fraction;
- with optimal L_{pm}, to optimize the L_{am} under varied primary flow liquid volume fraction.

2. CFD Modeling and Validation

The schematic of the ejector is presented in Figure 2 [15]. Its initial geometrical parameters are presented in Table 1, and boundary conditions are presented in Table 2.

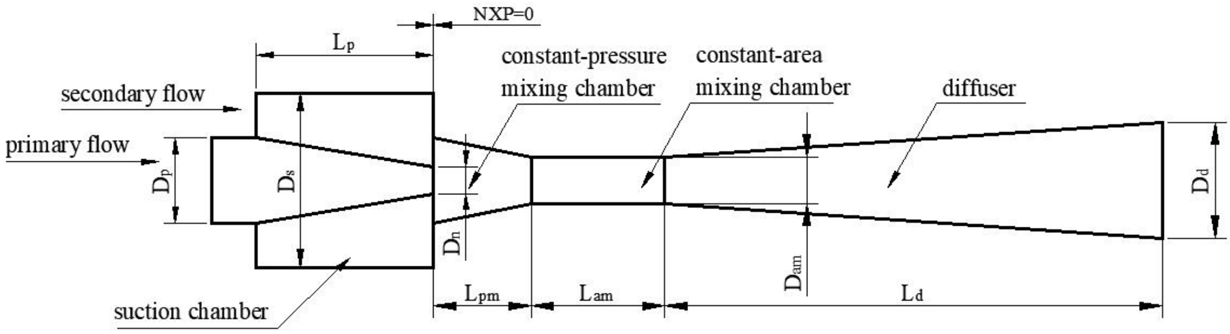

Figure 2. Schematic of the ejector.

Table 1. Initial geometrical parameters of the ejector.

Parameters	Value (mm)
The suction chamber diameter, D_s	19.6
The primary nozzle inlet diameter, D_p	9.6
The primary nozzle outlet diameter, D_n	3
The constant-area mixing chamber diameter, D_{am}	5.2
The diffuser outlet diameter, D_d	10
The primary nozzle length, L_p	20
The constant-pressure mixing chamber length, L_{pm}	11
The constant-area mixing chamber length, L_{am}	15
The diffuser length, L_d	56

Table 2. Boundary conditions for the ejector.

Parameters	Type	Pressure (kPa)	Temperature (K)	
			Superheated Gas	Two-Phase
Primary inlet	Pressure inlet	374.6	290	280
Secondary inlet	Pressure inlet	243.3	278	268
Outlet	Pressure outlet	267.63	-	-

To simulate the complex flow regime, the governing equations are the steady Reynolds Averaged Navier-Stokes equations [34,35].

Fluent 19.0 is used for the simulation. According to Palacz et al. [36], the differences in the results for the 3-D and 2-D models are negligible; therefore, the axisymmetric two-dimensional model is utilized in this CFD simulation. The properties of the working fluid are derived from NIST. Besagni et al. [37], Exposito-Carrillo et al. [38], and Croquer et al. [39] found that the k-omega SST model generally performed better in simulating the single-phase ejector; however, the realizable k-epsilon model is employed for two-phase ejector [35]. Meanwhile, near-wall refinement is used in the regions where large pressure and temperature gradient are possible to better capture shock waves and complex internal flow details. In addition, sensitivity analysis on wall treatments is performed and the first grid locates at 30 < y + < 300, which gives accurate results [15].

The PRESTO algorithm is applied to pressure-solving. Moreover, the second-order upwind discretization scheme is employed for density, momentum, energy, turbulent kinetic energy, and turbulent dissipation rate solving. All equations are iterated until the residuals are below 10–6. In addition, for an optimization study, consistent convergence of the CFD solution is sometimes difficult, especially when the solution is likely to be quasi-steady-state due to turbulence and the multi-phases. The convergence can often be slow, and the residual can remain stagnating or oscillating above-chosen convergence criteria.

Figure 3 presents the 2-D axisymmetric quadrilateral grid configuration for the baseline ejector. As shown in Figure 3, the pressure and velocity at Point A and Point B are used to detect the influence of the cell number. Tables 3 and 4 display the grid independence verification results. Pressure and velocity errors with area A and area B are less than 0.5%, indicating that the results are within the acceptable ranges; thus, the medium one with a grid number of 83,100 is selected.

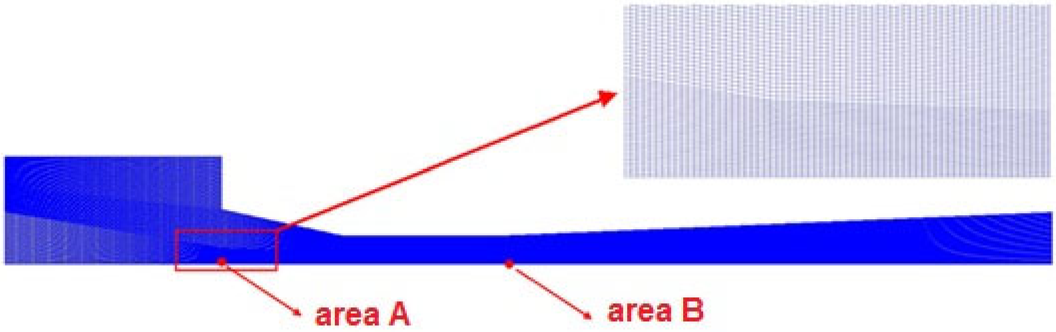

Figure 3. Densified meshes of the ejector.

Table 3. Mesh sensitivity analysis of area A.

Grid Number	Pressure (Pa)	Error (%)	Velocity (m·s^{-1})	Error (%)
52,200	274,947	-	120.138	-
68,520	275,288	0.12	119.893	0.2
83,100	275,521	0.085	119.684	0.17
114,880	275,613	0.033	119.623	0.051

Table 4. Mesh sensitivity analysis of area B.

Grid Number	Pressure (Pa)	Error (%)	Velocity (m·s^{-1})	Error (%)
52,200	206,538	-	165.218	-
68,520	206,879	0.165	164.934	0.172
83,100	207,054	0.085	164.841	0.056
114,880	207,123	0.033	164.788	0.032

The CFD model is validated by the void fraction inside the ejector which is based on the experimental results [15]. Take a typical case as an example, when LVF_1 is 0.1 and LVF_2 is 0. As shown in Figure 4, the maximum discrepancy is within 7.9%. The maximum deviation of α for many other ejector dimensions does not exceed 15%; thus, the model can be used in the following simulation.

As for the selection of a convergent nozzle, the comparison between the converging and the converging-diverging nozzle is presented below. For single-phase primary and secondary flow, based on the initial geometries, when the NXP is fixed at 0 mm and primary nozzle diverging section length is varied with 0 mm, 2 mm, 4 mm, and 6 mm, mass flow rates and ER are displayed in Figure 5. It is clear that, with the increase of the divergent section length, m_1 has little change, m_2 decreases significantly, and correspondingly, ER decreases with the increases in divergent section length. Moreover, the corresponding Mach number contours are shown in Figure 6. Hence, the converging nozzle is selected.

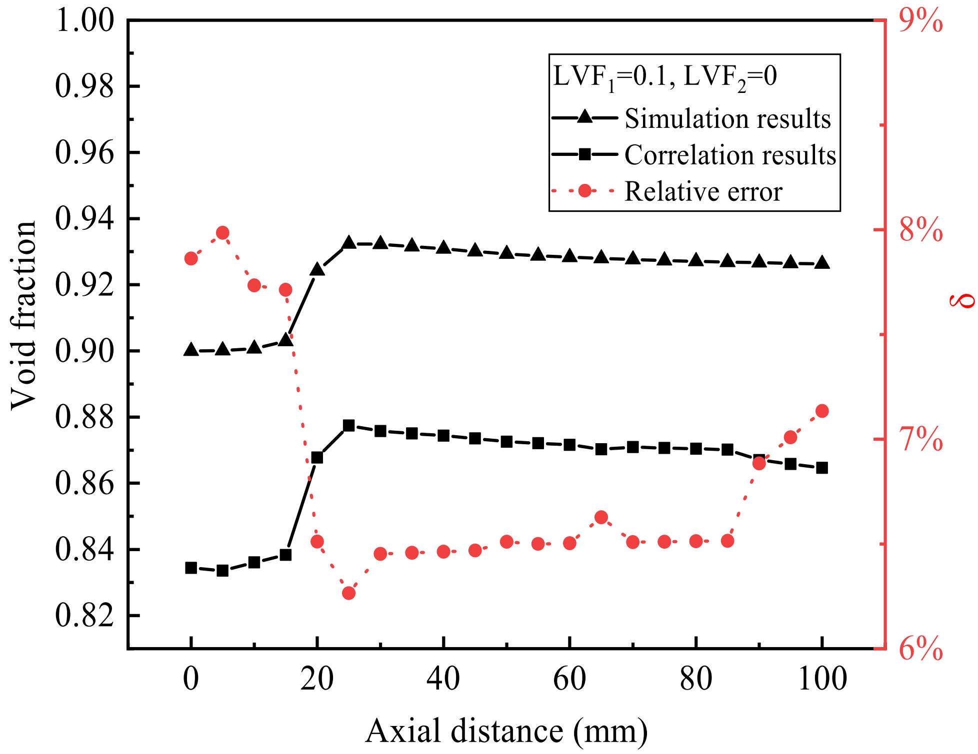

Figure 4. Comparison of α between simulation and correlation results.

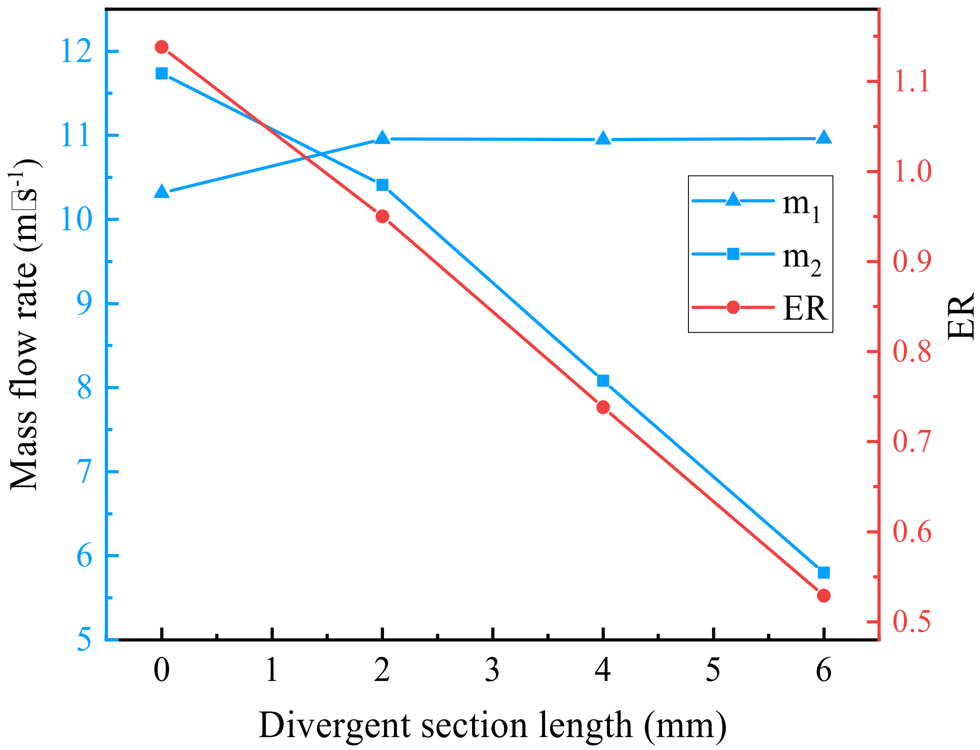

Figure 5. The relation of mass flow rate and ER with diverging section length of the primary nozzle.

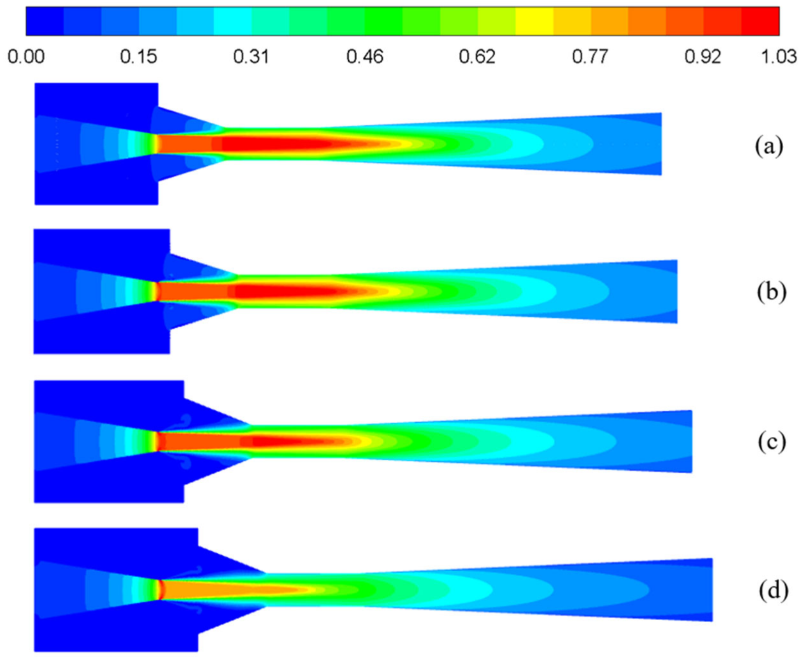

Figure 6. The Mach number contours under different nozzle diverging section lengths: (**a**) 0 mm; (**b**) 2 mm; (**c**) 4 mm; and (**d**) 6 mm.

3. Results and Discussion

3.1. Optimization of L_{pm}

3.1.1. Effect of Two-Phase Primary Flow

The L_{pm} is a key design parameter because it determines the mixing efficiency which indicates the ejector performance. Several groups of the L_{pm} are selected for analysis of the ejector performance under different LVFs of primary flow.

Figure 7 displays the ER with L_{pm} under LVF_2 = 0 and varied LVF_1 (the unfilled point indicates the baseline ejector model). It can be observed that for different LVF_1, ER always first rises moderately and then decreases steeply. To be specific, for LVF_1 of 0.02, when L_{pm} is increased from 8 mm to 50 mm, ER increases and peaks at L_{pm} of 23 mm which is magnified for the legend. After the peak value, ER drops slowly at first, then it falls suddenly, and even backflow occurs. Similarly, ER under LVF_1 of 0.04 also rises first and then reaches the peak of 0.237 at L_{pm} = 38 mm; the maximum ER increases by 26.58% over the baseline ejector. When LVF_1 are 0.06, 0.08, and 0.1, all the highest ER (0.145, 0.0922, and 0.0596, respectively) are achieved with L_{pm} of 44 mm. In addition, after the maximum value, the ER decreases suddenly to a negative value. To elucidate the abrupt drop of ER, contours of static pressure and axial static pressure distribution for the L_{pm} of 44 mm, 47 mm, and 50 mm are displayed in Figure 8a,b, respectively. Note that the amount of secondary fluid mass flow depends on how much pressure drop is induced at the outlet of the primary nozzle. Obviously, for L_{pm} = 44 mm, the static pressure rises smoothly, which can improve ejector performance. While for L_{pm} of 47 mm and 50 mm, higher pressure is generated, which weakens the ejector performance. When L_{pm} increases to 50 mm, the area of the high-pressure region increases, which further results in a decrease in ER. In addition, from another perspective, with the increase of L_{pm}, these two fluids mix more sufficiently, and correspondingly, the entrainment performance is enhanced; however, the increase of L_{pm} will also lead to the increase of frictional loss. Therefore, ejector performance suddenly decreases as L_{pm} increases to a certain value. As displayed by the velocity contours in Figure 8c, the energy loss increases largely when L_{pm} increases from 44 mm to 47 mm. For this purpose, L_{pm} should not exceed 44 mm for a proper operation of the ejector.

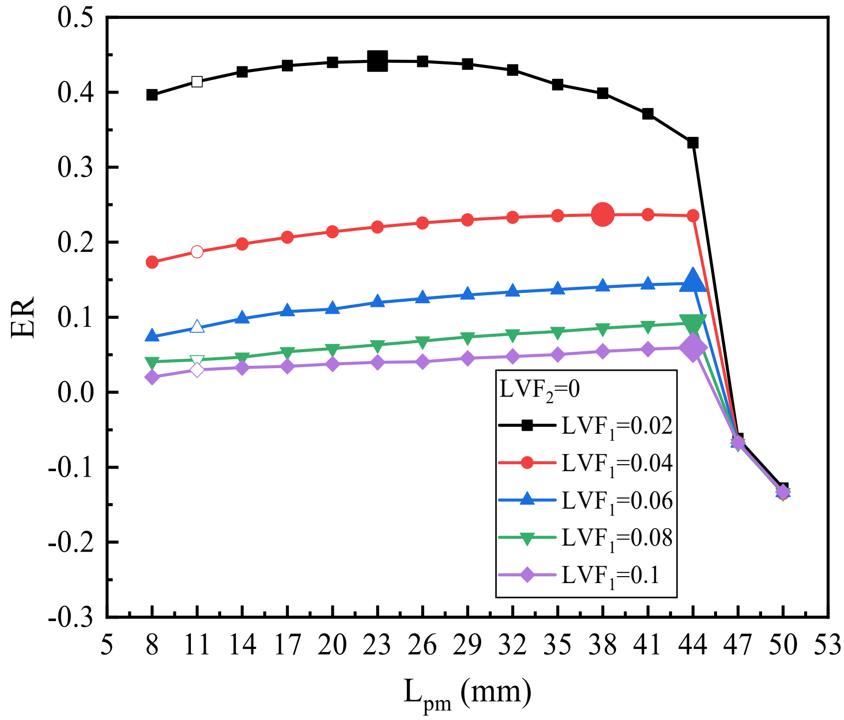

Figure 7. Optimization of L_{pm} on ER under LVF_1 = 0.02~0.1 (LVF_2 = 0).

In addition, compared with the baseline ejector model with an L_{pm} of 11 mm, the ejector under two-phase primary flow operation has a much longer optimal L_{pm}. That is to say, the optimal L_{pm} seriously deviates from the baseline ejector model, but when L_{pm} is more than 44 mm, the performance of the ejector drops drastically, which should be avoided.

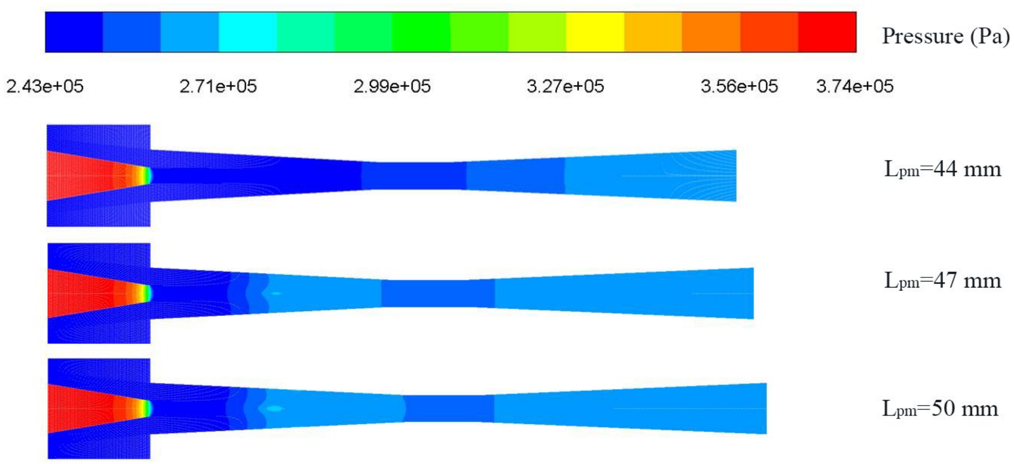

(a)

Figure 8. *Cont.*

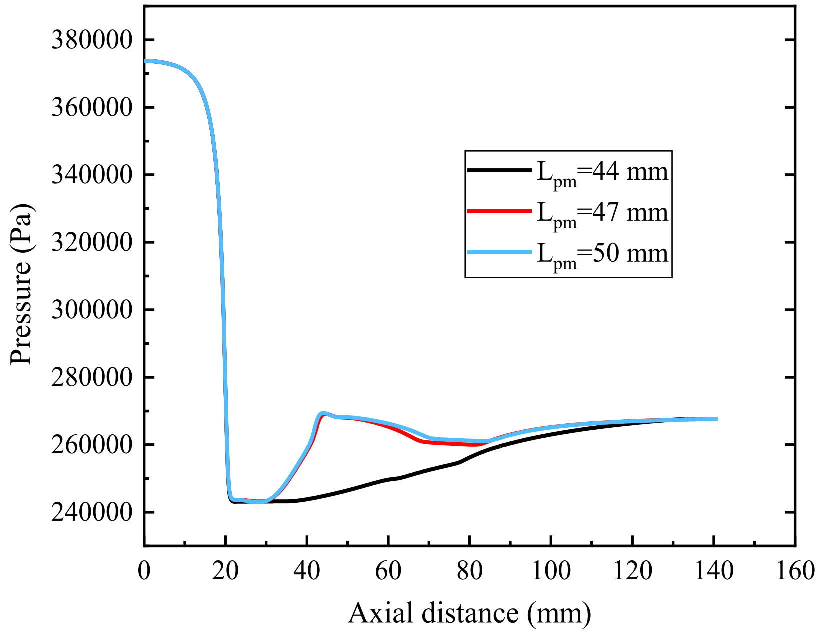

(**b**)

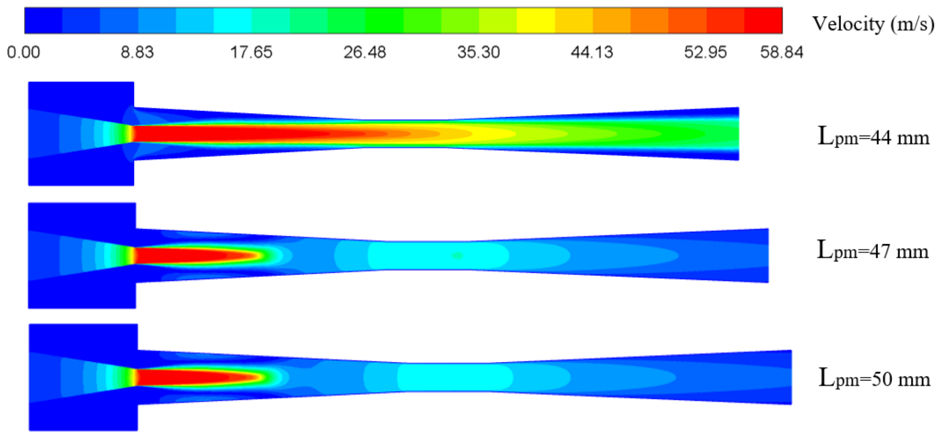

(**c**)

Figure 8. Pressure inside the ejector with different L_{pm} under LVF_1 = 0.06 and LVF_2 = 0: (**a**) Contour of static pressure; (**b**) Static pressure along the centerline; (**c**) Contour of velocity.

3.1.2. Effect of Two-Phase Secondary Flow

Optimization of L_{pm} under different LVF_2 and fixed LVF_1 of 0 is conducted in this section. Figure 9 portrays the change trends of ER with L_{pm}. To be specific, when LVF_2 is 0.02, ER first increases and then peaks at 1.99 when L_{pm} equals 5 mm. That is to say, for LVF_2 of 0.02, there exists an optimal L_{pm} of 5 mm, which is less than the L_{pm} of the baseline ejector of 11 mm. When LVF_2 varies from 0.04 to 0.1, all ERs rise first and then decrease with an increase in L_{pm}. Moreover, as displayed by the magnified point in Figure 9, the optimal L_{pm} are the same and all equal 2 mm, which is less than the L_{pm} of the baseline ejector as well. The maximum ERs are 2.36, 2.62, 2.78, and 2.91 for LVF_2 of 0.04, 0.06, 0.08, and 0.1, respectively, or the maximum ER increases with increasing LVF_2. Therefore, a higher ER is generated with a shorter L_{pm} under a two-phase secondary flow. Furthermore, it can be found that the optimal L_{pm} of a two-phase secondary flow is much shorter than the optimal L_{pm} of a two-phase primary flow.

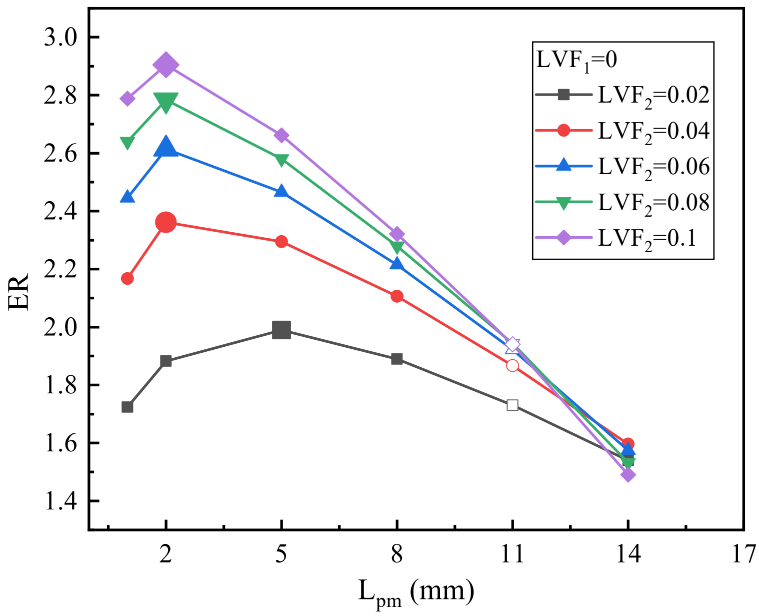

Figure 9. Optimization of L_{pm} on ER with LVF_1 = 0 and LVF_2 = 0.02~0.1.

With the results of Sections 3.1.1 and 3.1.2, the optimal L_{pm} is in the range of 23–44 mm when LVF_1 = 0.02~0.1 and LVF_2 = 0, and the longest optimal L_{pm} of 44 mm is obtained at LVF_1 = 0.1 and LVF_2 = 0. Moreover, the optimal L_{pm} is in the range of 2–5 mm when LVF_2 = 0.02~0.1 and LVF_1 = 0, and it can be said that the shortest optimal L_{pm} of 2 mm is obtained at LVF_1 = 0 and LVF_2 = 0.1. That is, when the LVF of both inlets are very different, the optimal L_{pm} also has a striking difference.

3.1.3. Effect of Two-Phase Primary and Secondary Flows

The above two sections are carried out under the circumstance that one of the ejector inlets does not contain liquid. Optimization of L_{pm} when both the primary and secondary flows contain liquid, by varying the LVF_1 and LVF_2, respectively, relevant simulation results are given below.

(a). Varied LVF_2 with fixed LVF_1

Figure 10 depicts the relationship between L_{pm} and ER under LVF_1 = 0.02 and LVF_2 = 0.02~0.1. It is readily found that for diversified LVF_2, ER always initially increases and then decreases along with the increase of L_{pm}. When LVF_2 changes from 0.04 to 0.1, the optimal L_{pm} are all 5 mm, which is less than the L_{pm} of the baseline ejector. The highest values of ER for LVF_2 from 0.04 to 0.1 are 1.65, 1.91, 2.07, and 2.2, respectively. In addition, in comparison with the baseline ejector, the corresponding maximum ERs increase by 6.64%, 13.58%, 16.81%, and 20.2%, respectively.

Figure 11 is the ER with L_{pm} under fixed LVF_1 of 0.06 and various LVF_2. For different LVF_2, ER always rises first and then consistently reduces along with the increase of L_{pm}. To be specific, for LVF_2 of 0.02, when L_{pm} increases from 2 mm to 20 mm, ER increases and arrives at its peak value of 0.68 at the L_{pm} of 17 mm. Furthermore, the maximum ER increases by 1.54% over the baseline ejector. Similarly, the changing trend of ER for LVF_2 = 0.04 is basically the same as that of LVF_2 = 0.02. The difference is that the optimal L_{pm} for LVF_2 = 0.04 is 11 mm, which is less than the L_{pm} of LVF_2 = 0.02. For LVF_2 of 0.06 and 0.08, both the peak values of ERs are obtained at the L_{pm} of 8 mm, which is less than the L_{pm} of the baseline ejector. Moreover, the maximum ER increases by 1.24% and 3.34%, respectively. As for the LVF_2 of 0.1, the maximum ER is 1.66 with the L_{pm} = 5 mm, and the maximum ER increases by 6.98%. It is worth mentioning that when L_{pm} deviates from the optimal value, the performance of the ejector will be greatly reduced. Furthermore, it is obviously observed that when LVF_2 increases, the optimal L_{pm} gets smaller. Compared with Figure 10, it can also be found that when LVF_1 increases from 0.02 to 0.06, for each LVF_2, the optimal L_{pm} increases a little.

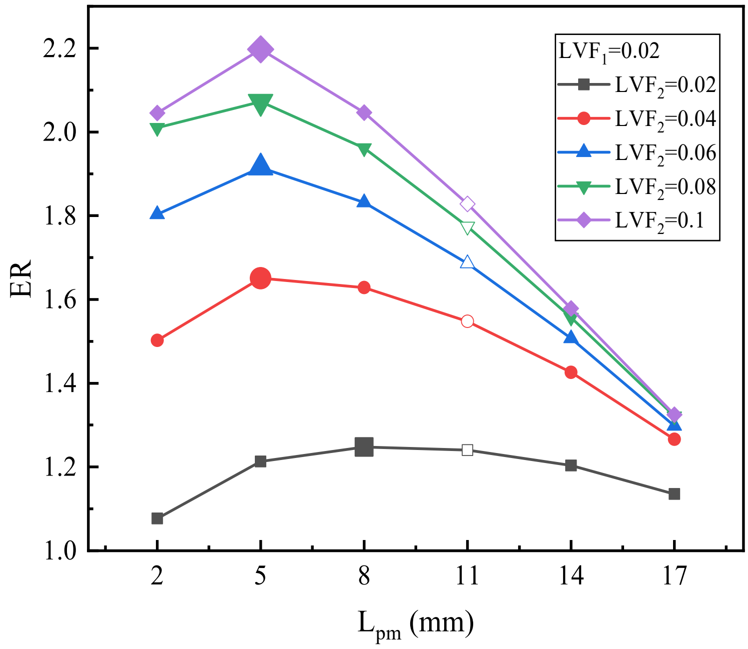

Figure 10. The relation of ER with L_{pm} under LVF_1 = 0.02 and LVF_2 = 0.02~0.1.

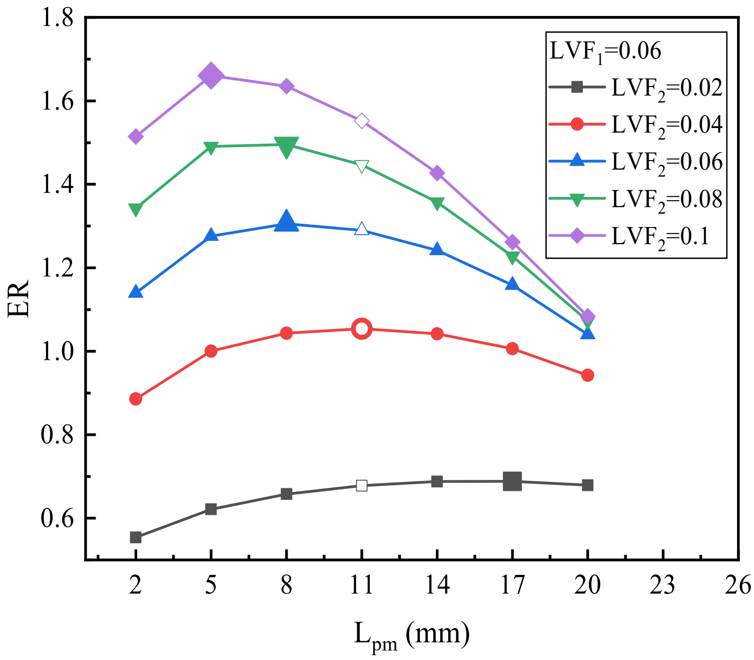

Figure 11. The relation of ER with L_{pm} under LVF_1 = 0.06 and LVF_2 = 0.02~0.1.

Figure 12 illustrates the changing trend of ER with L_{pm} under fixed LVF_1 of 0.1 and various LVF_2. For LVF_2 of 0.02, the maximum ER is 0.423 with L_{pm} = 23 mm, which increases by 9.59%. For LVF_2 of 0.04, the highest value of ER, 0.744, is achieved at the L_{pm} of 14 mm. Both for LVF_2 of 0.06 and 0.08, the maximum ERs (0.983 and 1.166, respectively) are obtained when L_{pm} reaches 11 mm. Moreover, similar to Figure 10, as LVF_2 increases from 0.02 to 0.1, the optimal L_{pm} is reduced gradually, since the optimal L_{pm} is 23 mm, 14 mm, 11 mm, 11 mm, and 8 mm, respectively. However, compared with Figure 10, namely when

LVF_1 increases from 0.06 to 0.1, for each fixed LVF_2, each optimal L_{pm} increases slightly, but the maximum ER drops.

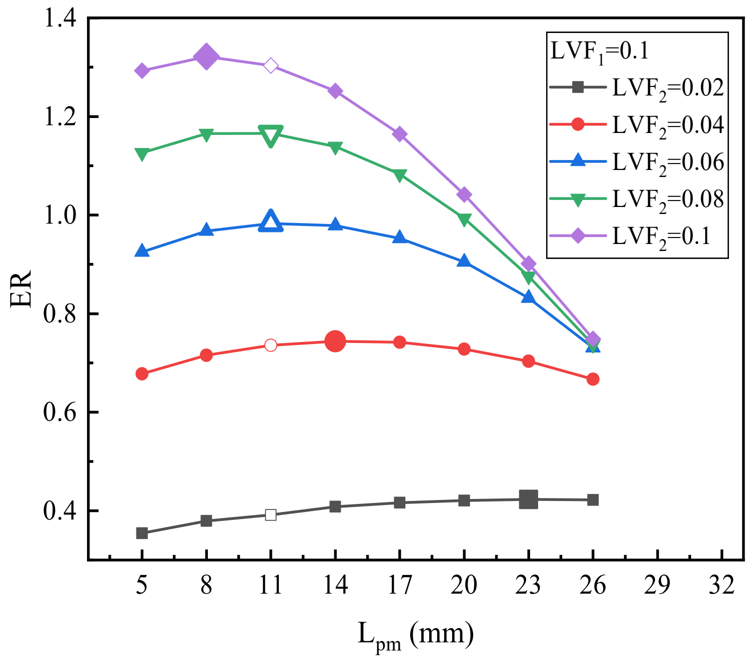

Figure 12. The relation of ER with L_{pm} under LVF_1 = 0.1 and various LVF_2.

In general, with the results of Figures 10–12, it can be concluded that: (1) for each fixed LVF_1, when LVF_2 increases from 0.02 to 0.1, the optimal L_{pm} decreases to different degrees; (2) the optimal L_{pm} is in 5–23 mm; (3) with the increases of LVF_1, the optimal L_{pm} generally increases; (4) combined with the operating condition of two-phase primary flow (LVF_2 = 0.02~0.1) as presented in Section 3.1.2, the optimal L_{pm} and ER decrease with an increase of LVF_1.

(b). Varied LVF_1 with fixed LVF_2

Figure 13 is the ER with L_{pm} under fixed LVF_2 of 0.02 and various LVF_1. Specifically speaking, for LVF_1 of 0.02, the ER reaches the peak value of 1.248 at L_{pm} = 8 mm. The maximum ER increases by 0.61% compared with the baseline ejector. In terms of LVF_1 = 0.04, the ER increases slightly from 0.844 to 0.907, after the highest value, ER drops gradually, and the optimal L_{pm} is 14 mm in this condition. When LVF_1 is in the range of 0.06 to 0.1, as L_{pm} increases, the increments of the ER do not change a lot. The optimal L_{pm} are 17 mm, 20 mm, and 23 mm for LVF_1 of 0.06, 0.08, and 0.1, respectively. The corresponding maximum ER increases by 1.54%, 3.34%, and 6.65%, respectively. Generally speaking, for LVF_2 of 0.02, as LVF_1 varies from 0.02 to 0.1, the optimal L_{pm}, as displayed by the magnified point in Figure 13, becomes larger and larger.

Figure 14 depicts the effect of L_{pm} on the ER under fixed LVF_2 of 0.06 and various LVF_1. ERs always increase initially and then decrease. To be specific, for LVF_1 of 0.02 and 0.04, both the ERs obtain the maximum value (1.915 and 1.544, respectively) at the L_{pm} of 5 mm, and the maximum ER increases by 13.58% and 4.17%, respectively. When LVF_1 changes from 0.08 to 0.1, ER increases along with the increase of L_{pm} and obtain the maximum of 1.12 and 0.98, respectively, both the optimum L_{pm} are 11 mm. Overall, when LVF_1 changes from 0.02 to 0.1, the optimal L_{pm} increases gradually, but all the optimal L_{pm} are no more than the L_{pm} of the baseline ejector. Compared with LVF_1 = 0.02 as displayed in Figure 13, when LVF_2 is 0.06, for each LVF_1, all the maximum ERs increase, but optimal L_{pm} decrease.

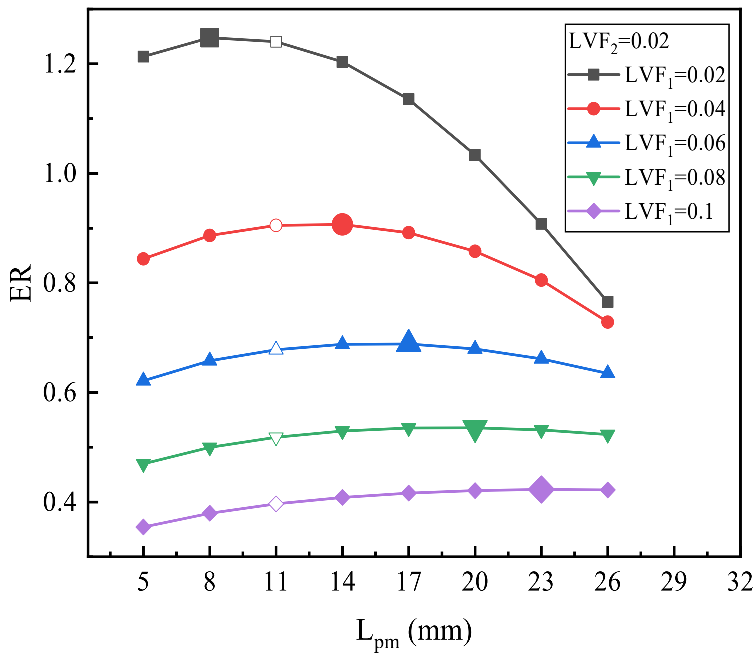

Figure 13. The relation of ER with L_{pm} under LVF_2 = 0.02 and LVF_1 = 0.02~0.1.

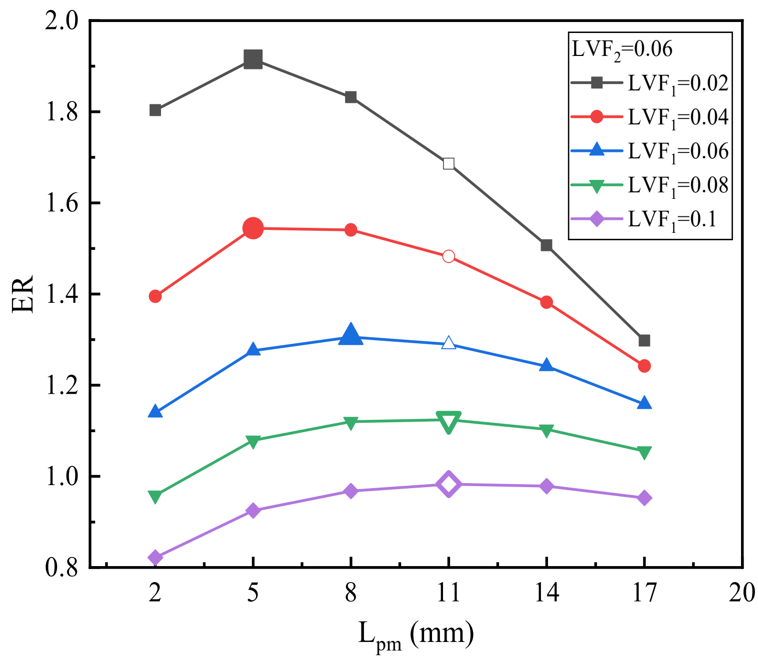

Figure 14. The relation of ER with L_{pm} under LVF_2 = 0.06 and LVF_1 = 0.02~0.1.

Figure 15 displays the impact of L_{pm} on the ER under LVF_2 = 0.1 and various LVF_1. The results reveal that all the Ers follow a similar pattern, namely, they increase first and then decrease with the growth of L_{pm}. For LVF_1 varied from 0.02 to 0.06, the maximum Ers (2.2, 1.9, and 1.66, respectively) are all achieved at the L_{pm} of 5 mm, which is slightly less than the baseline ejector. The maximum ER has an increase of 20.2%, 13.68%, and 6.98%, respectively. Moreover, when LVF_1 increases from 0.08 to 0.1, the optimal L_{pm} increases to 8 mm. The corresponding maximum ERs are 1.47 and 1.32 for LVF_1 of 0.08 and 0.1, respectively. In addition, the maximum ER increases by 3.01% and 1.4%, respectively. It is noteworthy that for fixed LVF_2 of 0.1 and various LVF_1, all the optimal L_{pm} are less than 11 mm. Compared with Figure 14 in which LVF_2 is 0.06, for each LVF_1, the maximum ER increases. Moreover, for LVF_1 = 0.06–0.1, the optimal L_{pm} also increases.

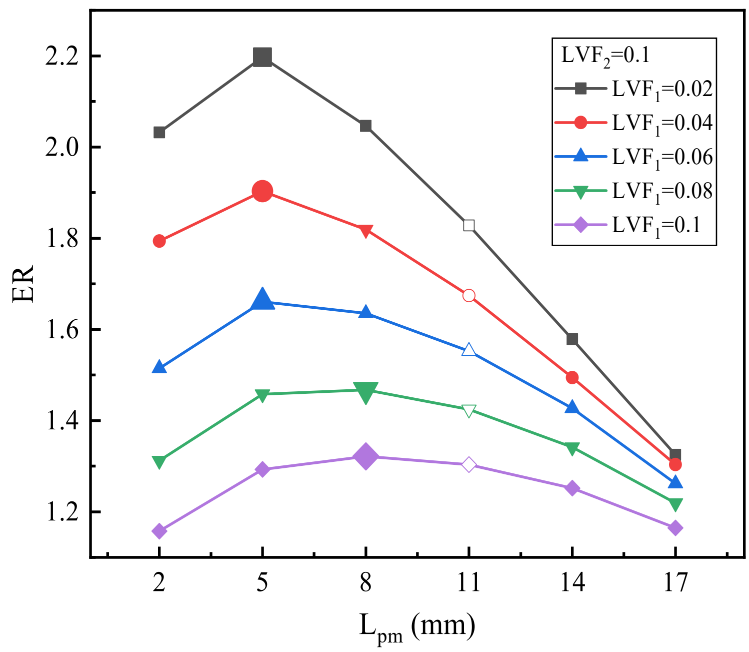

Figure 15. The variation of ER with L_{pm} under LVF_2 = 0.1 and LVF_1 = 0.02~0.1.

Overall, from Figures 13–15, it can be inferred that: (1) for each fixed LVF_2, the optimal L_{pm} increases with the growth of LVF_1; (2) with the increase of LVF_2, the optimal L_{pm} is generally reduced; (3) when both LVF_1 and LVF_2 are in the range of 0.02–0.1, the optimal L_{pm} is in the range of 5–23 mm; (4) and, combined with Figure 6 in which LVF_2 is 0, it can also be concluded that the when LVF_1 is fixed in the range of 0–0.1, the optimal L_{pm} improves with the growth of LVF_1, and the ER rises with the rise of LVF_2.

3.2. Optimization of L_{am}

Based on the optimal L_{pm} determined in Section 3.1, the following simulations are performed to seek the optimal L_{am}.

3.2.1. Effect of Two-Phase Primary Flow

Figure 16 reveals the influence of L_{am} on ER under various LVF_1 (LVF_2 = 0). For LVF_1 of 0.02 and 0.04, when L_{am} increases from 9 mm to 24 mm, the influence of L_{am} is not evident. The ER for LVF_1 = 0.02 increases from 0.438 at the L_{am} of 9 mm to the maximum of 0.442 at the L_{am} of 18 mm and then drops. For LVF_1 = 0.04, the ER rises first and reaches the maximum of 0.24 at L_{am} = 15 mm and then drops gradually. The optimal L_{am} for LVF_1 of 0.02 and 0.04 are 18 mm and 15 mm, respectively. For LVF_1 of 0.06 and 0.08, the optimal L_{am} are both 15 mm. Nonetheless, when L_{am} exceeds 15 mm, ER decreases abruptly. For LVF_1 of 0.1, the peak value of ER is 0.064 at the L_{am} of 18 mm, which means the LVF_1 = 0.1 has a more evident effect on the ER, the reason is that the liquid density is much higher than the vapor density. Likewise, after the peak value, ER drops suddenly. To avoid the malfunction of the ejector, the L_{am} should not exceed 15 mm, and the primary flow should not contain liquid. To identify the cause for the abrupt decrease, contours of static pressure, axial static pressure distribution, velocity contours, and the velocity vector field are displayed in Figure 17a–d, respectively. It can be observed from Figure 17a,b that the static pressure monotonically increases in the mixing chamber when L_{am} is 15 mm and 18 mm. In addition, when L_{am} rises to 21 mm, the mixed fluids have a momentum drop since the increase of the resistance weakens the ejector performance. In other words, when the friction loss caused by the increase of L_{am} exceeds the performance enhanced by the effect of more sufficient mixing, the ejector performance will decrease. Moreover, reflux occurs as illustrated in Figure 17d.

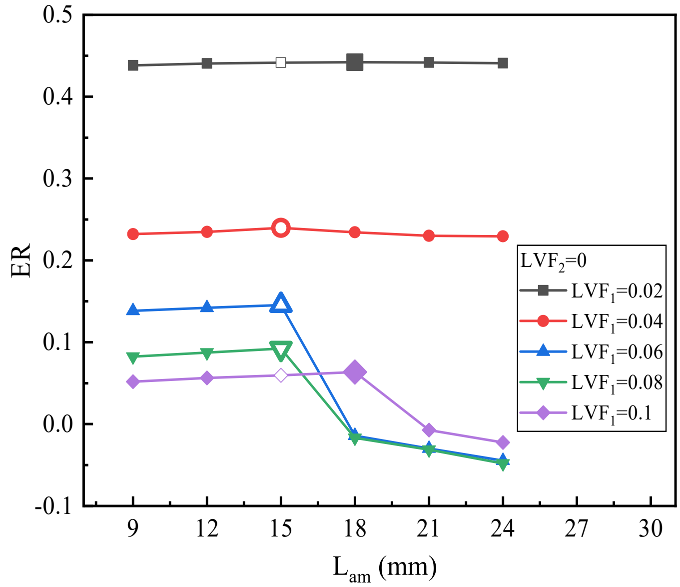

Figure 16. ER with L_{am} under LVF_1 = 0.02~0.1 (LVF_2 = 0).

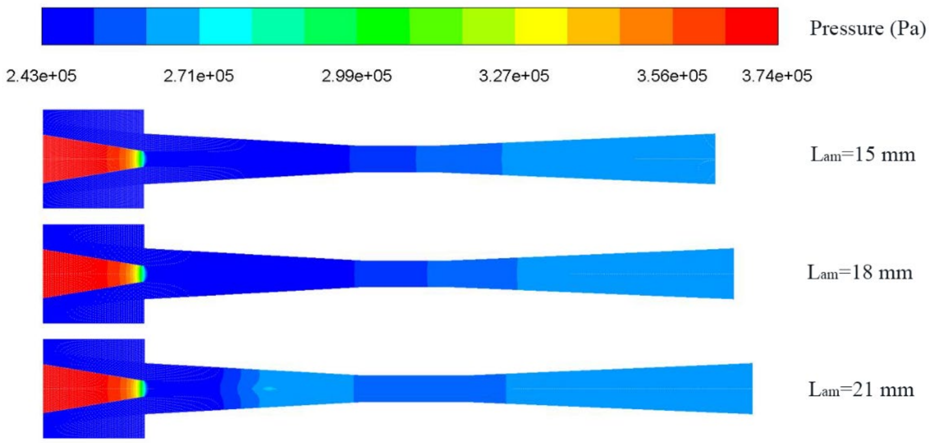

(**a**)

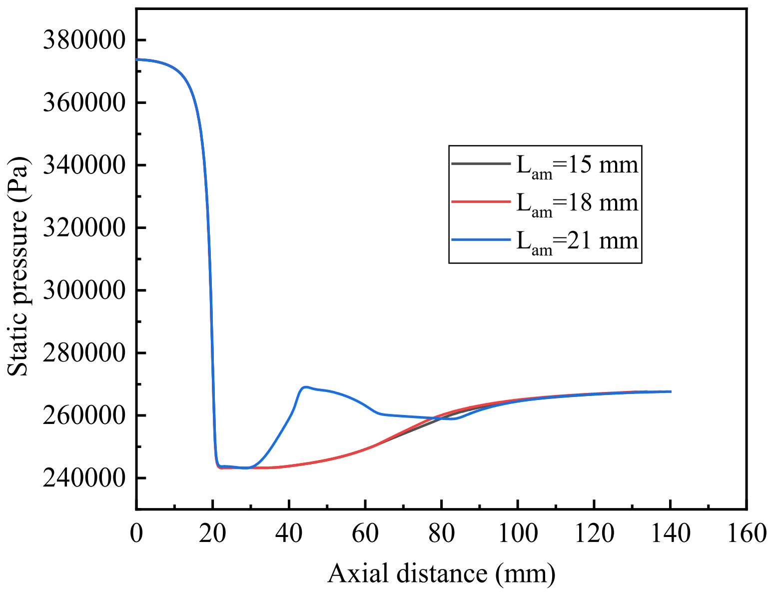

(**b**)

Figure 17. *Cont.*

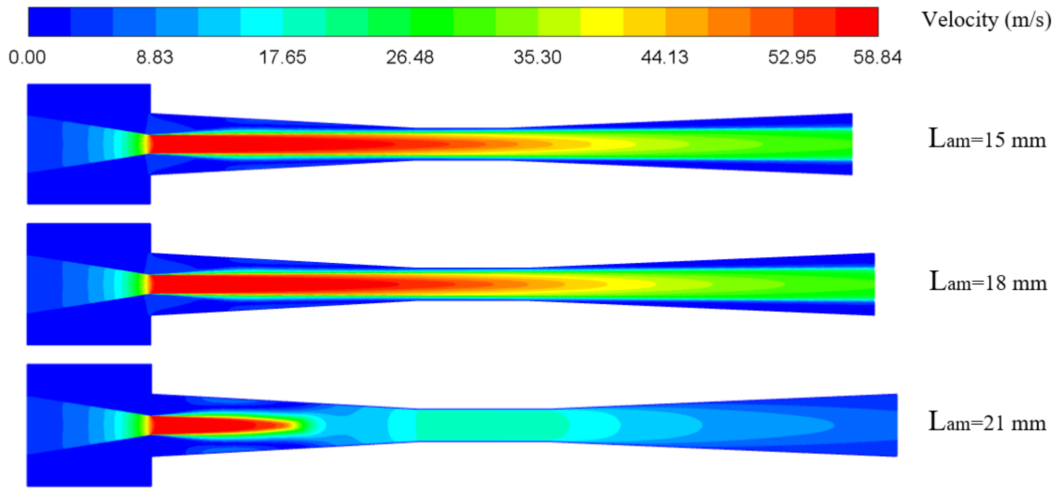

(**c**)

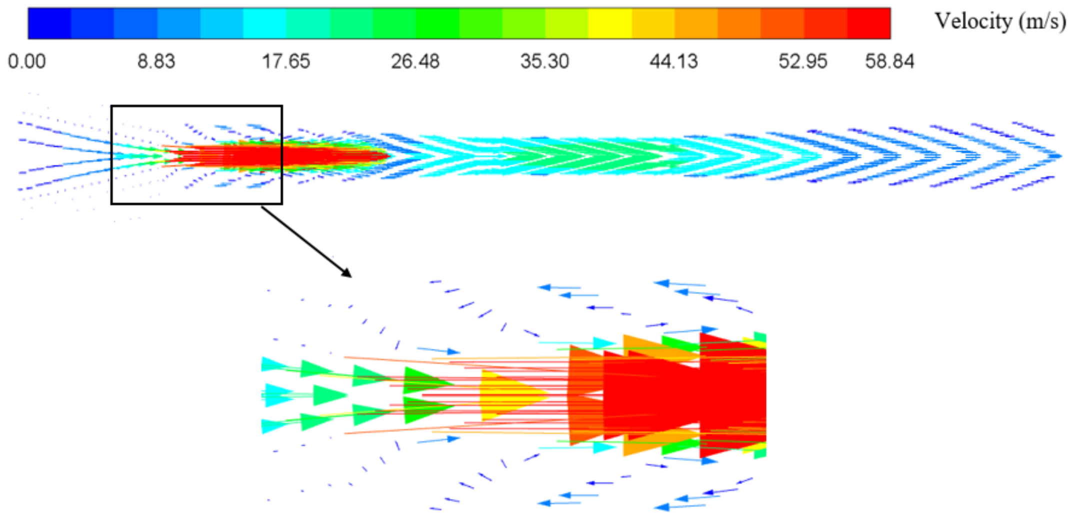

(**d**)

Figure 17. Pressure inside the ejector with different L_{am} under LVF_1 = 0.1 and LVF_2 = 0: (**a**) Contour of static pressure; (**b**) Static pressure along the centerline; (**c**) Contour of velocity and (**d**) Velocity vector field of L_{am} = 21 mm.

3.2.2. Effect of Two-Phase Secondary Flow

Figure 18 displays the effect of L_{am} on ER under fixed LVF_1 of 0 and various LVF_2. Obviously, under all the LVF_2, ER increases first and then decreases. Nevertheless, for various LVF_2, the optimal L_{am} is not always the same. Specifically, for LVF_2 = 0.02, the maximum ER of 2.02 peaks at the L_{am} of 12 mm. For LVF_2 = 0.04, the optimal L_{am} of 15 mm is the same as that of the baseline ejector. When LVF_2 is in the range of 0.06–0.1, the optimal L_{am} is at 9 mm.

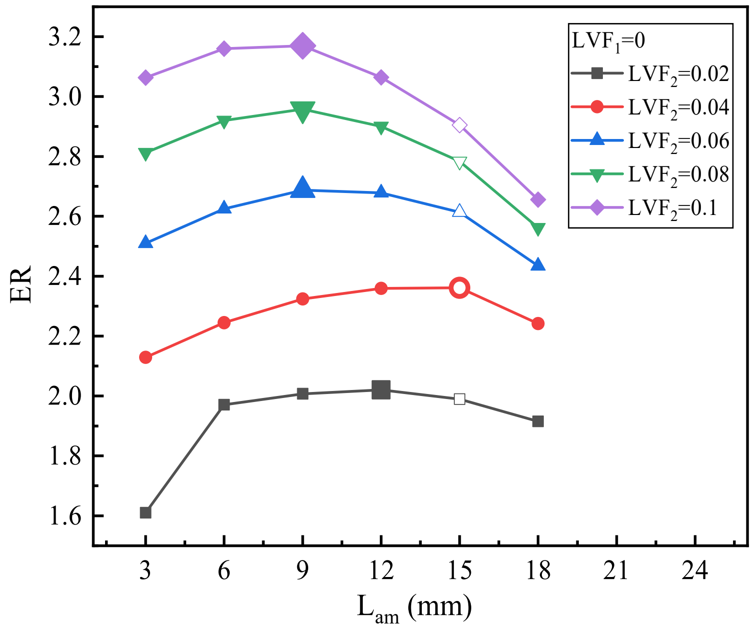

Figure 18. ER with L_{am} under LVF_2 = 0.02~0.1 (LVF_1 = 0).

3.2.3. Effect of Two-Phase Primary and Secondary Flows

All the L_{am} are optimized under LVF_1 = 0.02~0.1 and LVF_2 = 0.02~0.1 with an interval of 0.02. Considering the limited space, only two cases (LVF_1 = 0.1 and LVF_2 = 0.02~0.1, LVF_2 = 0.1 and LVF_1 = 0.02~0.1) are displayed here.

Figure 19 displays the effect of L_{am} on ER under fixed LVF_1 of 0.1 and various LVF_2 (0.02–0.1). When L_{am} increases from 6 mm to 21 mm, for a fixed LVF_2, the optimal L_{am} can be achieved.

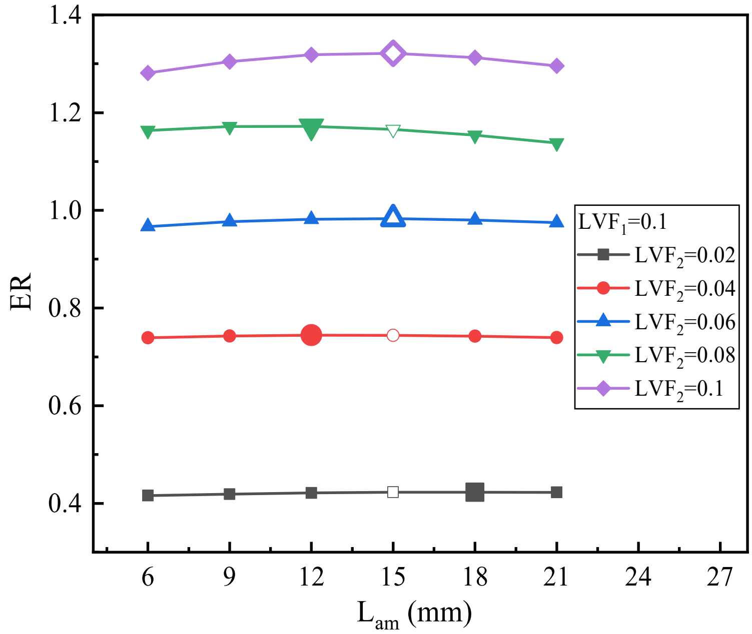

Figure 19. The relation of ER with L_{am} under LVF_1 = 0.1 and LVF_2 = 0.02~0.1.

Figure 20 presents the effect of L_{am} on ER under fixed LVF_2 of 0.1 and various LVF_1 (0.02–0.1). Obviously, for LVF_1 = 0.02, 0.04, and 0.06, it can be seen that the change in ER is relatively evident, while for LVF_1 = 0.08 and 0.1, the change in ER is pretty small. The results are similar to the variation of the optimal L_{am} with LVF in Figures 16, 18 and 19, namely the changing trend of optimal L_{am} is irregular.

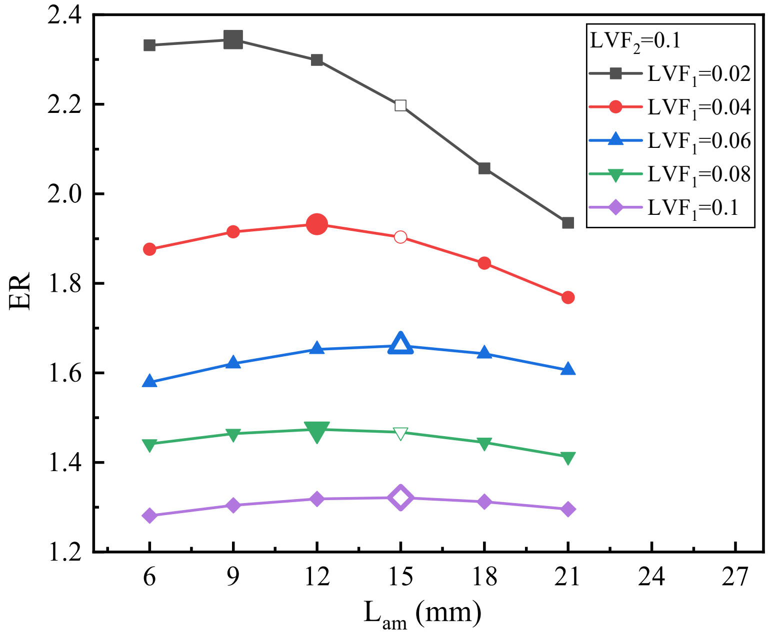

Figure 20. The relation of ER with L_{am} under LVF_2 = 0.1 and LVF_1 = 0.02~0.1.

In addition, the results of optimal L_{am} and ER under other LVF are presented in Tables 5 and 6.

Table 5. Results of optimal L_{am} and maximum ER under varied LVF_1 for a given LVF_2.

	LVF_2 = 0 (ER)	LVF_2 = 0.02 (ER)	LVF_2 = 0.06 (ER)	LVF_2 = 0.1 (ER)
LVF_1 = 0.02	18 (0.442)	15 (1.248)	12 (1.941)	9 (2.344)
LVF_1 = 0.04	21 (0.24)	9 (0.912)	15 (1.544)	12 (1.932)
LVF_1 = 0.06	15 (0.145)	6 (0.693)	15 (1.306)	15 (1.661)
LVF_1 = 0.08	15 (0.092)	12 (0.536)	12 (1.128)	12 (1.474)
LVF_1 = 0.1	18 (0.065)	18 (0.423)	15 (0.983)	15 (1.321)

Table 6. Results of optimal L_{am} and maximum ER under varied LVF_2 for a given LVF_1.

	LVF_1 = 0 (ER)	LVF_1 = 0.02 (ER)	LVF_1 = 0.06 (ER)	LVF_1 = 0.1 (ER)
LVF_2 = 0.02	12 (2.02)	15 (1.248)	6 (0.693)	18 (0.423)
LVF_2 = 0.04	15 (2.362)	15 (1.651)	12 (1.055)	12 (0.744)
LVF_2 = 0.06	9 (2.687)	12 (1.941)	15 (1.306)	15 (0.983)
LVF_2 = 0.08	9 (2.958)	9 (2.158)	12 (1.504)	12 (1.172)
LVF_2 = 0.1	9 (3.17)	9 (2.344)	15 (1.661)	15 (1.321)

With the results of Section 3.2, it can be found that the relation of optimal L_{am} with LVF_1 and LVF_2 is irregular since optimal L_{am} is influenced by optimal L_{pm}. When the optimal L_{pm} is more than 8 mm, the optimization of L_{am} is not evident, or the influence of L_{am} is not distinct. Nevertheless, when the optimal L_{pm} is less than 8 mm, the influence of L_{am} will be significant. The optimum L_{am} are in the range of 6–21 mm, and they do not deviate much from the L_{am} of the baseline ejector model (15 mm).

3.3. A Combination of Optimal L_{pm} and L_{am}

Figure 21 depicts the relation of the sum of optimal L_{pm} and L_{am} (L_{pam}) with LVF_2 under changed LVF_1. It can be observed that for each LVF_1, the optimal L_{pam} decreases with LVF_2. Furthermore, the optimal L_{pam} increases with LVF_1.

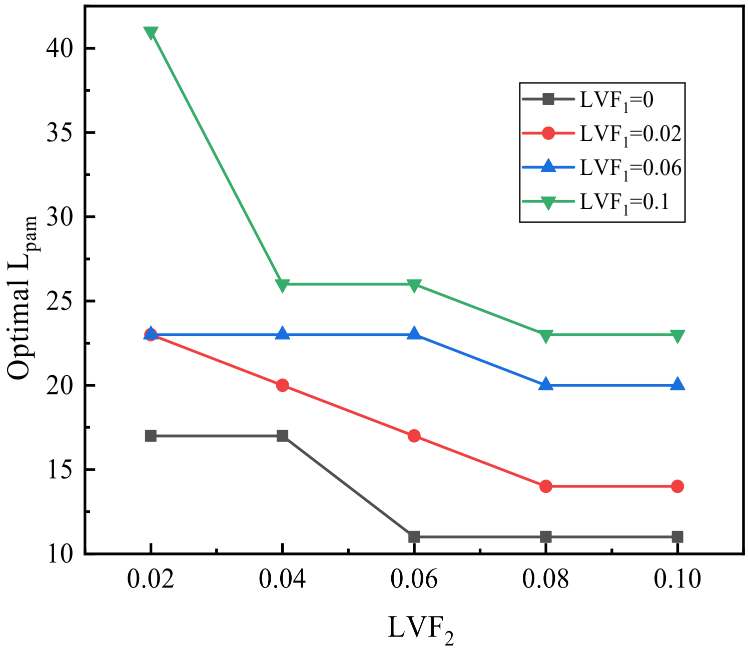

Figure 21. The relation of optimal L_{pam} with LVF_2 under different LVF_1.

Figure 22 indicates the relation of the sum of optimal L_{pm} and L_{am} with LVF_1 under different LVF_2. Generally speaking, the optimal L_{pam} increases with LVF_1 but reduces with LVF_2, and the relation between optimal L_{pm} and L_{pam} is regular.

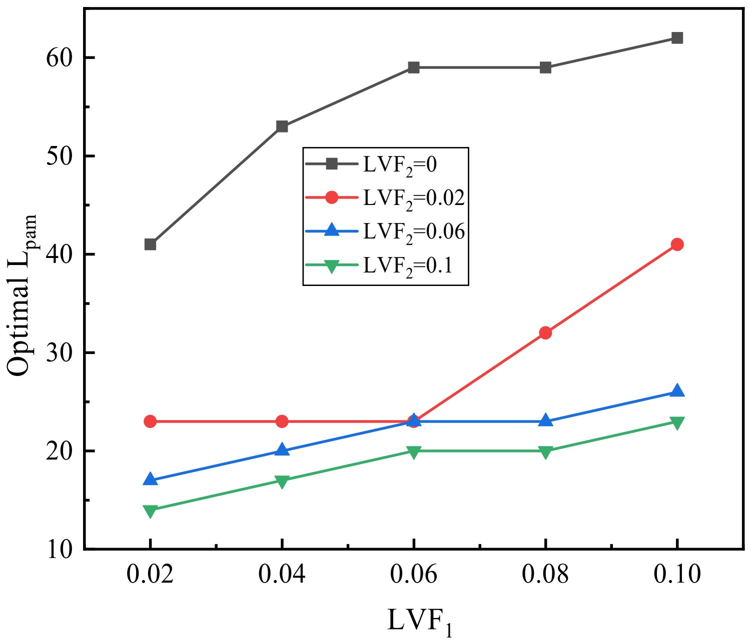

Figure 22. The relation of optimal L_{pam} with LVF_1 under given LVF_2.

4. Conclusions

This paper numerically optimizes two mixing chamber geometries of a two-phase ejector under various primary and secondary inlet LVFs. The most important findings are given below:

(1) When the primary inlet of the ejector contains liquid while the secondary inlet does not, the optimal L_{pm} and L_{am} are ranged between 23–44 mm and 15–18 mm. When the secondary inlet contains liquid while primary inlet does not, these two optimal lengths are ranged 2–5 mm and 9–15 mm, while when both the primary inlet and secondary inlet contain liquid, they are in the range of 5–23 mm and 6–18 mm, respectively. Thus, two mixing chamber lengths largely depend on the vapor or liquid state of the two inlets;

(2) When primary inlet LVF is fixed and secondary inlet LVF increases from 0 to 0.1, the optimal L_{pm} decreases along with the growth of secondary inlet LVF; when secondary inlet LVF is fixed and primary inlet LVF varies from 0 to 0.1, the optimal L_{pm} increases along with the growth of primary inlet LVF;

(3) The sum of optimal L_{pm} and optimal L_{am} increases with the increase of primary inlet LVF but decreases with the increase of secondary inlet LVF.

Author Contributions: Conceptualization, J.Y. and J.J.; methodology, H.W.; investigation, J.Y.; writing—original draft preparation, H.W.; writing—review and editing, Y.S. All authors have read and agreed to the published version of the manuscript.

Funding: The research was funded by the Educational Department of Sichuan Province, China (Funding No.: 17ZB0449).

Institutional Review Board Statement: Not applicable.

Informed Consent Statement: Not applicable.

Conflicts of Interest: The authors declare no conflict of interest.

Nomenclature

L_{pm}	constant-pressure mixing chamber length, mm
L_{am}	constant-area mixing chamber length, mm
L_{pam}	sum of mixing chamber length, mm
P	pressure, kPa
T	temperature, K or °C
m_1	primary mass flow rate, $g \cdot s^{-1}$
m_2	secondary mass flow rate, $g \cdot s^{-1}$
χ	quality
α	void fraction
AR	area ratio
ER	entrainment ratio
PRR	pressure recovery ratio
LVF_1	liquid volume fraction of primary flow
LVF_2	liquid volume fraction of secondary flow
NXP	nozzle exit position
MERS	multi-evaporator refrigeration system

References

1. Besagni, G.; Mereu, R.; Inzoli, F. Ejector refrigeration: A comprehensive review. *Renew. Sustain. Energy Rev.* **2016**, *53*, 373–407. [CrossRef]
2. Wang, J.; Qv, D.; Yao, Y.; Ni, L. The difference between vapor injection cycle with flash tank and intermediate heat exchanger for air source heat pump: An experimental and theoretical study. *Energy* **2021**, *221*, 119796. [CrossRef]
3. Cuong, L.N.; Oh, J.T. The Comparison of Experiment Results and CFD Simulation in the Heat Pump System Using Thermobank and Two-Phase Ejector for Heating Room and Cold Storage. *Int. J. Air-Cond. Refrig.* **2016**, *24*, 1650004. [CrossRef]

4. Shi, Y.; Guo, X.; Zhang, X. Study on Economized Vapor Injection Heat Pump System Using Refrigerant R32. *Int. J. Air-Cond. Refrig.* **2016**, *24*, 1650006. [CrossRef]
5. Gullo, P.; Kærn, M.R.; Haida, M.; Smolka, J.; Elbel, S. A review on current status of capacity control techniques for two-phase ejectors. *Int. J. Refrig.* **2020**, *119*, 64–79. [CrossRef]
6. Chen, Q.; Hwang, Y.; Yan, G.; Yu, J. Theoretical investigation on the performance of an ejector enhanced refrigeration cycle using hydrocarbon mixture R290/R600a. *Appl. Therm. Eng.* **2020**, *164*, 114456. [CrossRef]
7. Dokandari, D.A.; Khoshkhoo, R.H.; Bidi, M.; Mafi, M. Thermodynamic investigation and optimization of two novel combined power-refrigeration cycles using cryogenic LNG energy. *Int. J. Refrig.* **2021**, *124*, 167–183. [CrossRef]
8. Barta, R.B.; Dhillon, P.; Braun, J.E.; Ziviani, D.; Groll, E.A. Design and Optimization Strategy for Ejectors Applied in Refrigeration Cycles. *Appl. Therm. Eng.* **2021**, *189*, 116682. [CrossRef]
9. Liu, J.; Lin, Z. A novel dual-temperature ejector-compression heat pump cycle-exergetic and economic analyses. *Int. J. Refrig.* **2021**, *126*, 155–167. [CrossRef]
10. Elliott, M.S.; Rasmussen, B.P. Decentralized model predictive control of a multi-evaporator air conditioning system. *Control Eng. Pract.* **2013**, *21*, 1665–1677. [CrossRef]
11. Li, C.; Yan, J.; Li, Y.; Cai, W.; Lin, C.; Chen, H. Experimental study on a multi-evaporator refrigeration system with variable area ratio ejector. *Appl. Therm. Eng.* **2016**, *102*, 196–203. [CrossRef]
12. Li, S.; Yan, J.; Liu, Z.; Yao, Y.; Li, X.; Wen, N.; Zou, G. Optimization on crucial ejector geometries in a multi-evaporator refrigeration system for tropical region refrigerated trucks. *Energy* **2019**, *189*, 116347. [CrossRef]
13. Yan, J.; Li, S.; Li, R. Numerical study on the auxiliary entrainment performance of an ejector with different area ratio. *Appl. Therm. Eng.* **2020**, *185*, 116369. [CrossRef]
14. Wen, N.; Wang, L.; Yan, J.; Li, X.; Liu, Z.; Li, S.; Zou, G. Effects of operating conditions and cooling loads on two-stage ejector performances. *Appl. Therm. Eng.* **2019**, *150*, 770–780. [CrossRef]
15. Wen, H.; Yan, J.; Li, X. Influence of liquid volume fraction on ejector performance: A numerical study. *Appl. Therm. Eng.* **2021**, *190*, 116845. [CrossRef]
16. Kumar, V.; Sachdeva, G. 1-D model for finding geometry of a single phase ejector. *Energy* **2018**, *165*, 75–92. [CrossRef]
17. Ramesh, A.S.; Sekhar, S.J. Experimental and numerical investigations on the effect of suction chamber angle and nozzle exit position of a steam-jet ejector. *Energy* **2018**, *164*, 1097–1113. [CrossRef]
18. Palacz, M.; Haida, M.; Smolka, J.; Nowak, A.J.; Banasiak, K.; Hafner, A. HEM and HRM accuracy comparison for the simulation of CO_2 expansion in two-phase ejectors for supermarket refrigeration systems. *Appl. Therm. Eng.* **2017**, *115*, 160–169. [CrossRef]
19. Aidoun, Z.; Ameur, K.; Falsafioon, M.; Badache, M. Current advances in ejector modeling, experimentation and applications for refrigeration and heat pumps. Part 2: Two-phase ejectors. *Inventions* **2019**, *4*, 16. [CrossRef]
20. Fu, W.; Li, Y.; Liu, Z.; Wu, H.; Wu, T. Numerical study for the influences of primary nozzle on steam ejector performance. *Appl. Therm. Eng.* **2016**, *106*, 1148–1156. [CrossRef]
21. Chunnanond, K.; Aphornratana, S. Ejectors: Applications in refrigeration technology. *Renew. Sustain. Energy Rev.* **2004**, *8*, 129–155. [CrossRef]
22. Jeon, Y.; Kim, D.; Jung, J.; Jang, D.S.; Kim, Y. Comparative performance evaluation of conventional and condenser outlet split ejector-based domestic refrigerator-freezers using R600a. *Energy* **2018**, *161*, 1085–1095. [CrossRef]
23. Tang, Y.; Liu, Z.; Li, Y.; Huang, Z.; Jon, K. Study on fundamental link between mixing efficiency and entrainment performance of a steam ejector. *Energy* **2021**, *215*, 119128. [CrossRef]
24. Nakagawa, M.; Marasigan, A.R.; Matsukawa, T.A. Kurashina, Experimental investigation on the effect of mixing length on the performance of two-phase ejector for CO_2 refrigeration cycle with and without heat exchanger. *Int. J. Refrig.* **2011**, *34*, 1604–1613. [CrossRef]
25. Sarkar, J. Ejector enhanced vapor compression refrigeration and heat pump systems—A review. *Renew. Sustain. Energy Rev.* **2012**, *16*, 6647–6659. [CrossRef]
26. Banasiak, K.; Hafner, A.; Andresen, T. Experimental and numerical investigation of the influence of the two-phase ejector geometry on the performance of the R744 heat pump. *Int. J. Refrig.* **2012**, *35*, 1617–1625. [CrossRef]
27. Jeon, Y.; Kim, S.; Kim, D.; Chung, H.J.; Kim, Y. Performance characteristics of an R600a household refrigeration cycle with a modified two-phase ejector for various ejector geometries and operating conditions. *Appl. Energy* **2017**, *205*, 1059–1067. [CrossRef]
28. Fu, W.; Liu, Z.; Li, Y.; Wu, H.; Tang, Y. Numerical study for the influences of primary steam nozzle distance and mixing chamber throat diameter on steam ejector performance. *Int. J. Therm. Sci.* **2018**, *132*, 509–516. [CrossRef]
29. Dong, J.; Hu, Q.; Yu, M.; Han, Z.; Cui, W.; Liang, D.; Ma, H.; Pan, X. Numerical investigation on the influence of mixing chamber length on steam ejector performance. *Appl. Therm. Eng.* **2020**, *174*, 115204. [CrossRef]
30. Hemidi, A.; Henry, F.; Leclaire, S.; Seynhaeve, J.M.; Bartosiewicz, Y. CFD analysis of a supersonic air ejector. Part I: Experimental validation of single-phase and two-phase operation. *Appl. Therm. Eng.* **2009**, *29*, 1523–1531. [CrossRef]
31. Yuan, G.; Zhang, L.; Zhang, H.; Wang, Z. Numerical and experimental investigation of performance of the liquid-gas and liquid jet pumps in desalination systems. *Desalination* **2011**, *276*, 89–95. [CrossRef]
32. Chen, W.; Huang, C.; Bai, Y.; Chong, D.; Yan, J.; Liu, J. Experimental and numerical investigation of two phase ejector performance with the water injected into the induced flow. *Int. J. Adv. Nucl. React. Des. Technol.* **2020**, *2*, 15–24. [CrossRef]

33. Aliabadi, M.A.F.; Bahiraei, M. Effect of water nano-droplet injection on steam ejector performance based on non-equilibrium spontaneous condensation: A droplet number study. *Appl. Therm. Eng.* **2021**, *184*, 116236. [CrossRef]
34. Yan, J.; Li, S.; Liu, Z. Numerical investigation on optimization of ejector primary nozzle geometries with fixed/varied nozzle exit position. *Appl. Therm. Eng.* **2020**, *175*, 115426. [CrossRef]
35. Li, C.; Li, Y.Z. Investigation of entrainment behavior and characteristics of gas-liquid ejectors based on CFD simulation. *Chem. Eng. Sci.* **2011**, *66*, 405–416. [CrossRef]
36. Palacz, M.; Smolka, J.; Kus, W.; Fic, A.; Bulinski, Z.; Nowak, A.J.; Banasiak, K.; Hafner, A. CFD-based shape optimisation of a CO2 two-phase ejector mixing section. *Appl. Therm. Eng.* **2016**, *95*, 62–69. [CrossRef]
37. Besagni, G.; Cristiani, N.; Croci, L.; Guédon, G.R.; Inzoli, F. Computational fluid-dynamics modelling of supersonic ejectors: Screening of modelling approaches, comprehensive validation and assessment of ejector component efficiencies. *Appl. Therm. Eng.* **2021**, *186*, 116431. [CrossRef]
38. Carrillo, J.A.E.; de la Flor, F.J.S.; Lissén, J.M.S. Single-phase ejector geometry optimisation by means of a multi-objective evolutionary algorithm and a surrogate CFD model. *Energy* **2018**, *164*, 46–64. [CrossRef]
39. Croquer, S.; Poncet, S.; Aidoun, Z. Turbulence modeling of a single-phase R134a supersonic ejector. Part 1: Numerical benchmark. *Int. J. Refrig.* **2016**, *61*, 140–152. [CrossRef]